

# Effects of strain amplitude, cycle number and orientation on low cycle fatigue microstructures in austenitic stainless steel studied by electron channelling contrast imaging

J. Nellessen, S. Sandlöbes\* and D. Raabe

*Max-Planck-Institut für Eisenforschung GmbH, Department for Microstructure Physics and Alloy Design, 40237 Düsseldorf, Germany*

Received 21 August 2014; revised 10 December 2014; accepted 14 December 2014

**Abstract**—Substructure analysis on cyclically deformed metals is typically performed by time-consuming transmission electron microscopy probing, thus limiting such studies often to a single parameter. Here, we present a novel approach which consists in combining electron backscatter diffraction (EBSD), digital image correlation and electron channelling contrast imaging (ECCI), enabling us to systematically probe a large matrix of different parameters with the aim of correlating and comparing their interdependence. The main focus here is to identify the influence of cycle number, initial grain orientation and local strain amplitude on the evolving dislocation patterns. Therefore, experiments up to 100 cycles were performed on a polycrystalline austenitic stainless steel with local strain amplitudes between 0.35% and 0.95%. EBSD and ECCI maps reveal the individual influence of each parameter while the others remained constant. We find that the dislocation structures strongly depend on grain orientation. Dislocation structures in grains with double-slip ( $\langle 112 \rangle // \text{LD}$ ,  $\langle 122 \rangle // \text{LD}$  and  $\langle 012 \rangle // \text{LD}$ ) and multiple-slip ( $\langle 111 \rangle // \text{LD}$ ,  $M \langle 011 \rangle // \text{LD}$  and  $\langle 001 \rangle // \text{LD}$ ) orientations with respect to the loading direction (LD) are characterized under the variation of strain amplitude and cycle number.  
 © 2014 Acta Materialia Inc. Published by Elsevier Ltd. All rights reserved.

**Keywords:** Low cycle fatigue (LCF); Dislocation structures; Electron channelling contrast imaging (ECCI); Stainless steel

## 1. Introduction

Austenitic stainless steels are key materials in multiple structural, industrial infrastructure and energy applications. During operation these structural components are subjected to reversed plasticity due to cyclic thermal stresses. Low cycle fatigue (LCF) represents a predominant loading and failure mode. Hence, it is essential to understand the microstructural evolution during cyclic deformation [1–5].

During the past decades, substantial progress has been made in studying the fatigue properties and underlying mechanisms of different alloys. Many studies were performed on pure face-centred cubic (fcc) materials, particularly on Cu single crystals [6–9]. The results of these studies were summarized by Basinski and Basinski [10] and more recently by Li et al. [11]. However, only few fundamental studies were performed on more complex materials such as stainless steels [2,12–24].

Although cyclic deformation is very sensitive to a number of parameters such as temperature, strain amplitude, stacking fault energy, orientation and loading conditions, most studies so far focused on the microstructure evolution

as a function of a single parameter. Such single-parameter studies addressed effects of temperature [3,5,13,15], strain amplitude [2,3,14,16,18,20,21,25], cycle number [22–24], strain rate [1] and interstitial alloying [26,27] on the microstructure evolution during cyclic loading. Up to now, no studies have been performed on the combined and interactive influence of these parameters.

Similarly, most studies on the formation of dislocation structures during cyclic deformation of stainless steels were performed on high (>1000 cycles) cycle numbers or were conducted after failure [12,14,15,17,18]. However, the dislocation arrangements change significantly during the early stages of cyclic fatigue, as was recently pointed out by Pham et al. [22–24].

Surprisingly, no studies on the orientation dependence of dislocation structure formation during cyclic fatigue are available for stainless steels although such an influence was revealed by a number of studies on pure fcc metal single crystals such as Cu [28–32] or polycrystalline Ni [33].

The aim of this study is to investigate the orientation dependence of the formation of dislocation substructures during low cycle fatigue under systematic variation of strain amplitude and cycle number. We apply an integrated approach using combined electron backscatter diffraction (EBSD), digital image correlation (DIC) and electron channelling contrast imaging (ECCI). The setup is designed in such a way, that a limited set of experiments is sufficient

\* Corresponding author. Tel.: +49 02116792162; fax: +49 02116792333; e-mail: [s.sandloebes@mpie.de](mailto:s.sandloebes@mpie.de)

to screen a large parameter matrix including systematic combinations of strain amplitude, cycle number and crystallographic orientations.

## 2. Experimental procedure

The material investigated is austenitic stainless steel of type AISI316, Table 1. The microstructure is fully austenitic with a grain size of 60  $\mu\text{m}$  and random crystallographic texture.

Bone-shaped flat specimens with a gauge length of 8 mm, a width of 2 mm and a thickness of 1 mm were prepared via spark-erosion. Prior to deformation the specimens were mechanically ground and polished.

Fig. 1 shows an example of the applied sequence of experiments. First, crystallographic characterization of all specimens was performed using EBSD, Fig. 1a. The EBSD scans were performed on a CamScan 4 tungsten-filament scanning electron microscope with an acceleration voltage of 20 kV and a step size of 3  $\mu\text{m}$ . Cyclic deformation experiments were performed with a Kammrath & Weiss tensile-compression module equipped with a 5 kN load cell under displacement control ( $\pm 100 \mu\text{m}$ ) with a strain rate of  $0.5 \times 10^{-3} \text{ s}^{-1}$  (Fig. 1b).

A three-dimensional DIC setup by GOM (Gesellschaft für Optische Messtechnik) was used to measure the local strain distribution in situ during cyclic deformation. The cyclic experiments were conducted for 30, 50 and 100 cycles and the subsequent analysis of the local strain distribution was performed using the DIC analysis software Aramis (GOM) [34,35]. The effective local strain amplitude was calculated for the complete specimen and averaged over equidistant regions of 500  $\mu\text{m}$  (Fig. 1c). We use the term “local strain amplitude” when referring to strain amplitudes calculated in this way throughout this paper. The upper image in Fig. 1c shows an exemplary DIC snapshot of the local strain distribution after one half-cycle; the colour code and values displayed in the corresponding legend refer only to the relative local strains of this particular half-cycle with respect to the initial half-cycle. The local strain amplitudes were calculated from the sum of all cycles. The lower graph in Fig. 1c shows the local strain amplitudes for different DIC measurement points along the specimen loading axis. The information of the average local strain amplitude obtained by DIC analysis was superimposed with the EBSD maps (Fig. 1d). By applying this procedure, defined regions were mapped in which both, the averaged local strain amplitude and the crystallographic orientation, of individual grains were known.

Detailed post mortem ECCI observations were performed in grains with three different double-slip ( $\langle 112 \rangle // \text{LD}$ ,  $\langle 122 \rangle // \text{LD}$  and  $\langle 012 \rangle // \text{LD}$ ) and three different multiple-slip ( $\langle 111 \rangle // \text{LD}$ ,  $\langle 011 \rangle // \text{LD}$  and  $\langle 001 \rangle // \text{LD}$ ) orientations, with effective local strain amplitudes of 0.35%, 0.65% and 0.95%, respectively, and for specimens subjected

to 30, 50 and 100 cycles, respectively. This observation matrix contains 54 different combinations of strain amplitude, cycle number and crystallographic orientation ( $3 \times 3 \times 6$ ). We performed 158 individual measurement (on average three different areas per parameter combination) to ensure that the observed dislocation structures are consistent. The presented data are typical results for the respective combinations of strain amplitude, cycle number and orientation. By using in situ DIC during deformation it was possible to select grains with different orientations and local strain amplitudes from one specimen. This allows the systematic analysis of a high number of parameters by using a limited number of specimens. All orientations probed in this study refer to the standard triangle shown in Fig. 1e; the discussion of crystallographic equivalent orientations is based on this Schmid-type notation. This procedure enables the systematic evaluation of a matrix that includes 54 different combinations of strain amplitude, cycle number and grain orientation. Observation of the dislocation arrangements in each probed grain was performed using ECCI in a high-resolution field emission gun scanning electron microscope (Zeiss FIB XB1540) using a working distance of  $\sim 6 \text{ mm}$  and an acceleration voltage of 30 kV without any repolishing after deformation to preserve surface steps formed by planar dislocation slip. All dislocation structures originate from regions inside the grains and not from regions close to grain boundaries.

ECCI observations of cycled specimens give two important sets of information on the same specimen: (i) slip traces of active dislocations are visible as surface steps (straight lines in Fig. 2) and enable us to determine the active slip planes with the largest shear contribution; (ii) the formed debris dislocation structures in the microstructure after the preceding loading step are visible simultaneously [36–41], Fig. 4. Hence, the direct relation between the active slip systems and the formed dislocation structures is possible.

## 3. Experimental results

### 3.1. Global strain behaviour and mechanical response

The strain amplitude for all experimentally probed microstructure patches was calculated based on the locally obtained DIC results, which enables us to extract the local deformation state in different cross-sectional zones, Figs. 1c and 3. We have observed strain inhomogeneities also along the vertical direction; however, the vertical strain inhomogeneities are not as pronounced as the horizontal strain inhomogeneities. A detailed analysis of the vertically aligned DIC points clearly reveals strain inhomogeneities in the order of 10% with respect to the average strain amplitude at this position. We interpret this difference with respect to the loading direction. The loading direction is parallel to the specimen axis; therefore the stress component in the horizontal direction is higher than in the vertical direction and consequently also the strain inhomogeneities. We observed that the average global strain amplitude remains constant over all cycles. When compared to classical strain-controlled experiments performed by other groups, e.g. Refs. [4,42] using similar global strain amplitudes, it was confirmed that the cyclic hardening curves obtained by displacement controlled experiments are comparable, Fig. 2.

**Table 1.** Material composition in wt.%.

Cr	Ni	Mo	Mn	Si	N
17.2	12.2	2.48	1.44	0.389	0.088
P	C	O	Al	S	Fe
0.036	0.0249	0.0076	<0.005	0.0008	Bal.

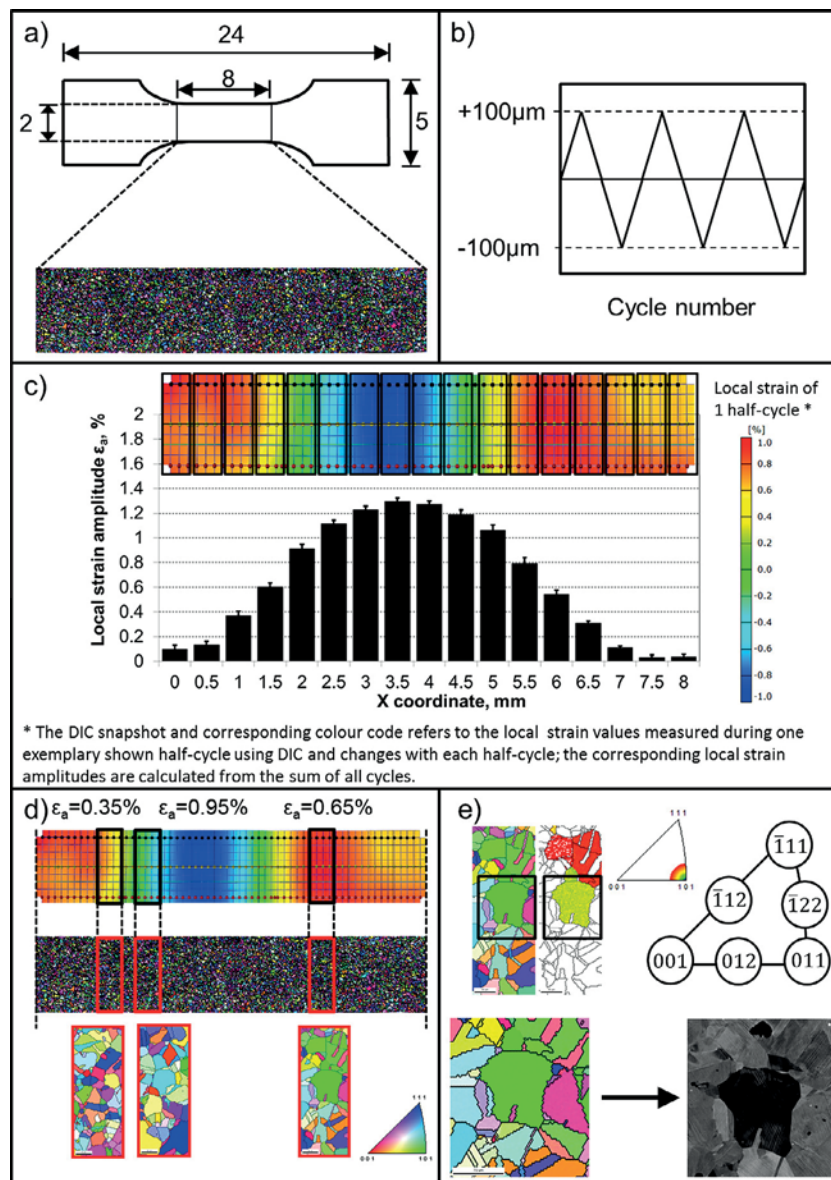


**Fig. 1.** Overview of the experimental procedure. (a) Prior to cyclic deformation the specimens were measured by EBSD to obtain the crystallographic orientations. (b) Afterwards the specimens were cyclically deformed to up to 100 cycles under displacement control. (c) In situ strain analyses by DIC was performed during cyclic deformation showing a variation of the local strain amplitude along the loading axis ( $X$  coordinate), the example shown being for one half-cycle; the colour code and values in the legend refer only to this particular half-cycle with respect to the initial state; the local strain amplitudes shown in the graph are calculated from the sum of all cycles. (d) Correlation of EBSD and DIC results considering the local (and not the global) strain amplitude was performed. (e) ECCI channelling was conducted on selected crystallographic orientations for different local strain amplitudes, respectively. (For interpretation of the references to colour in this figure legend, the reader is referred to the web version of this article.)

### 3.2. Local strain distribution and local strain amplitude

Fig. 3 exemplarily shows the distribution of the local strain along the specimen dimensions and corresponding local strain amplitude curves for different regions along the loading axis (areas A, B, C, D and E in Fig. 3) over 100 cycles. The results reveal that the averaged global strain amplitude is not consistent with the effective local strain amplitude. Specifically, the local strain amplitude is inhomogeneously distributed along the specimen loading axis (Fig. 3).

To verify that these strain inhomogeneities are genuine, we have (i) repeated the experiments, (ii) compared the global cyclic hardening curves with classical strain-controlled

experiments performed by other groups [4,42] (Fig. 2) and (iii) performed experiments on Al single crystals where we found significantly less inhomogeneous strain distributions. These results strongly indicate that the observed strain inhomogeneities are real and result from the fact that the local stress state may profoundly deviate from the macroscopic loading state in polycrystalline aggregates. Consequently, strain and hardening evolve differently depending on the respective local stress state. This assumption is further supported by the local strain amplitude curves shown in Fig. 3: sample regions which experience higher local strain amplitudes (areas C and D) show an earlier and more pronounced hardening and softening during cycling than regions which experience lower local strain amplitudes.



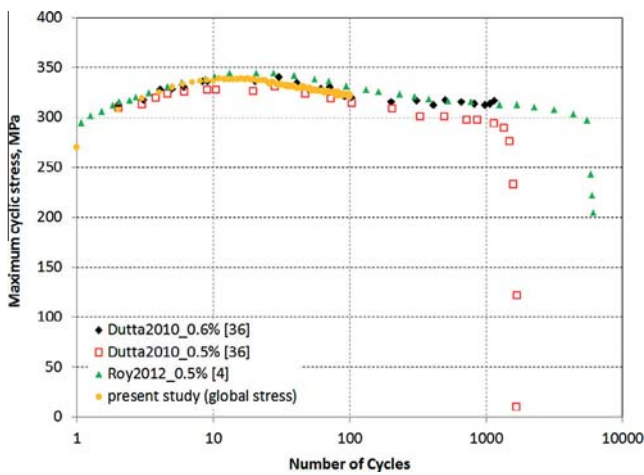


Fig. 2. Global cyclic hardening response obtained in this study in comparison to strain-controlled experiments with similar strain amplitudes performed by other groups [4,36].

Specifically, the curve for the lowest local strain amplitude (region E) decreases constantly up to  $\sim 40$  cycles and then remains almost constant, indicating that this region is still in the local hardening stage. For the regions with

intermediate local strain amplitudes (A, B, C) the local hardening stage is earlier completed. The strain amplitude in regions A and B constantly decreases up to 20–25 cycles, and then remains nearly constant, indicating that they are at the transition from hardening to softening after 100 cycles. In region C the local hardening is completed after 15–20 cycles followed by a local softening. In region D the local softening starts after 10 cycles.

These macroscopically (DIC scale) measured strain inhomogeneities stem most probably from local, i.e. microscopical, strain inhomogeneities due to locally different stress states arising during polycrystalline deformation. Due to their different orientation some grains are more favourably oriented for dislocation glide than others. Consequently, localized plastic deformation takes place and stress concentrations and strain gradients occur. This results in locally different cyclic hardening and softening behaviour during fatigue. EBSD results indicate that the observed (DIC scale) strain inhomogeneities are even higher at the grain scale. Such plastic inhomogeneities have also been reported by Jiang [43]. Hence, the observed dislocation structures cannot be simply related to the average global strain amplitude – as measured without using DIC – but are sensitively depending on the micromechanical, i.e. local, stress state and the resulting local strain amplitude.

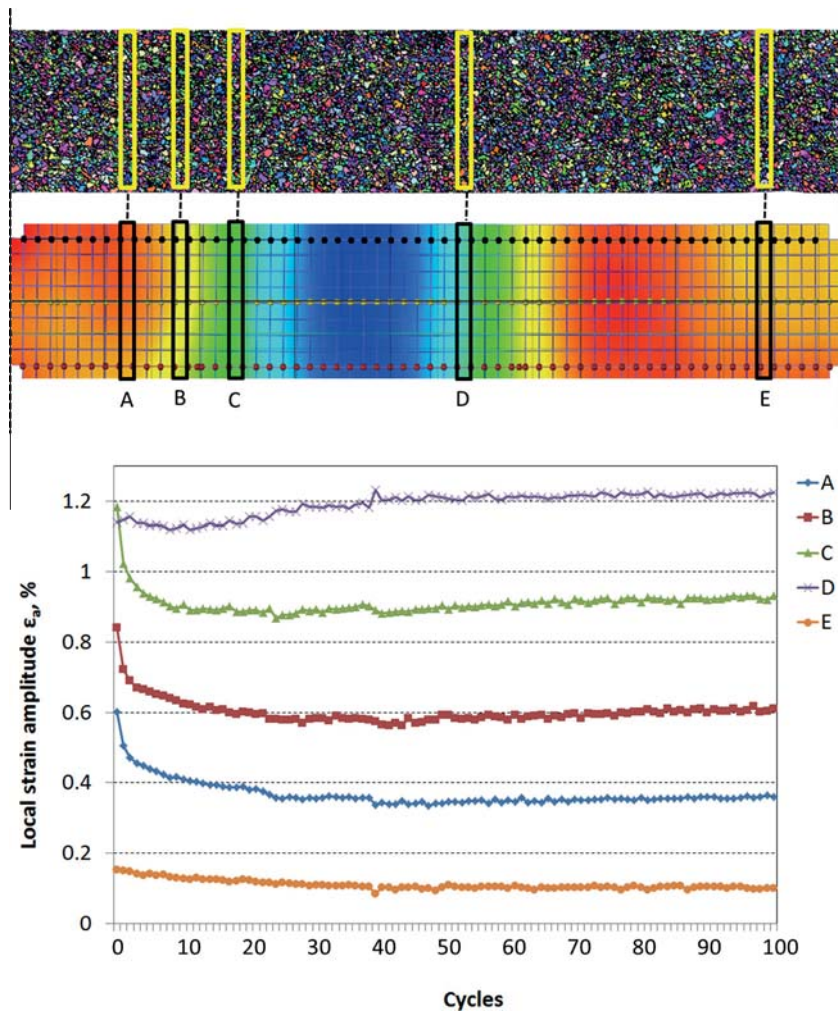
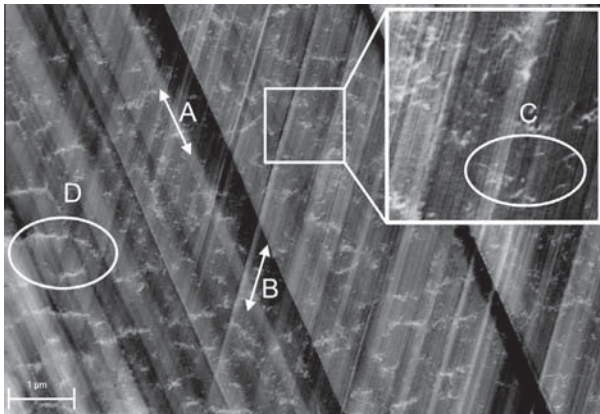


Fig. 3. DIC snapshot showing the observed heterogeneous strain distribution along the specimen loading axis and corresponding local strain amplitude curves for different regions (areas A, B, C, D and E) over 100 cycles.



**Fig. 4.** Observation of features by ECI: surface traces of different active slip planes (A, B), individual dislocations (C) (enlarged region) and dislocation structures such as veins (D).

### 3.3. Microstructural evolution

#### 3.3.1. $\langle 112 \rangle$ LD double-slip orientation

Fig. 5 shows the dislocation arrangements for double-slip orientations close to  $\langle 112 \rangle$  // LD. The dislocation arrangement for a strain amplitude of 0.35% (Fig. 5a–c) consists mainly of individual dislocations, the majority of which is aligned with the observed slip traces. No significant increase in the dislocation density is observed with an increasing number of cycles. The traces of two slip planes are observed.

Fig. 5d–f ( $\epsilon_a = 0.65\%$ ) reveals an increase in planar dislocation activity with increasing strain amplitude, as visible from the higher density and narrower slip plane traces and an overall increased dislocation density when compared to regions exposed to  $\epsilon_a = 0.35\%$ . After 30 cycles, mainly individual dislocations which are aligned with the slip traces are present, whereas after 50 cycles dislocation clusters with dimensions 100–200 nm have formed. After 100 cycles these clusters appear much more homogeneous, indicating the beginning of vein formation, i.e. clear dislocation-rich regions (pre-veins) are separated by dislocation-depleted regions (channels). The cluster size roughly equals their spacing. Similarly to the observations at  $\epsilon_a = 0.35\%$  the traces of at least two active slip planes are visible, of which one system appears to be dominant for all considered strain amplitudes and cycle numbers.

After 30 cycles and a strain amplitude of 0.95% the dislocation density (Fig. 5g) is significantly higher than for lower strain amplitudes and dislocation clusters are observed. After 50 cycles (Fig. 5h) these clusters transform into inhomogeneously distributed “pre-veins”. After 100 cycles (Fig. 5i), clear and well defined veins with a thickness of 100–200 nm and a distance of 0.5–1.0 μm have formed. These veins are elongated along three different directions, parallel to the traces of (101),  $(\bar{1}01)$  and either  $(\bar{2}\bar{1}1)$  or  $(3\bar{1}0)$  planes. Contrast changes within one grain indicate heterogeneous strain distribution inside the grain and subgrain formation. As observed for a strain amplitude of 0.65%, the dominance of one set of slip plane traces is also confirmed for a strain amplitude of 0.95%, although further slip traces are present but less pronounced.

#### 3.3.2. $\langle 122 \rangle$ // LD double-slip orientation

Fig. 6 shows the dislocation arrangements formed inside orientations that are close to  $\langle 122 \rangle$  // LD. Similar to the structures formed in  $\langle 122 \rangle$  // LD orientations, individual dislocations aligned with the slip traces of active slip planes are present. A slight increase in dislocation density was found with increasing cycle number.

Both the dislocation density and the activity of planar slip increased when exposed to higher strain amplitudes. After 100 cycles inhomogeneous dislocation arrangements are observed: in some parts of the grain vein formation sets in, while in other regions individual dislocations or clusters prevail. This finding is more pronounced in the case of 0.95% strain amplitude where a band of pronounced veins coexists with regions where individual dislocations are observed. The size of the veins in Fig. 6i amounts to 100–200 nm with a spacing of 0.2–0.6 μm, respectively. Since the veins are not well-developed, an unambiguous identification of their crystallographic direction alignment was not possible. However, individual segments were found to be preferentially aligned parallel to (110) plane traces. Also, vein segments parallel to (113), (001) or  $(\bar{3}\bar{3}2)$  plane traces were observed.

#### 3.3.3. $\langle 012 \rangle$ // LD double-slip orientation

Fig. 7 shows the observed dislocation arrangements observed in double-slip orientations close to  $\langle 012 \rangle$  // LD.

Individual dislocations are the predominant feature observed at a strain amplitude of 0.35%. The dislocations are either randomly distributed or aligned along the traces of the active slip planes. Increasing planar slip activity which is apparent in terms of a higher density of slip traces is observed with increasing strain amplitude. For this regime ( $\epsilon_a = 0.65\%$ ) the dislocation density increased after 30 cycles. After 50 cycles dislocation clusters with a size of 100–200 nm and a distance of 100–500 nm have formed. The structure shown in Fig. 7f ( $N = 100$ ) marks the transition from clusters to “loose” veins but no pronounced channels are observed. When compared to 50 cycles the size of the “pre-veins” formed after 100 cycles remains at an average value of 100–200 nm but the distance between them increases slightly up to 400–500 nm. The dislocation structures for a strain amplitude of 0.95% are similar to those formed at a strain amplitude of 0.65%, but with a more pronounced vein structure.

#### 3.3.4. $\langle 111 \rangle$ // LD multiple-slip orientation

The dislocation arrangements formed in grains with multiple-slip orientations close to  $\langle 111 \rangle$  // LD are shown in Fig. 8. At a strain amplitude of 0.35% individual dislocations prevail after 30 and 50 cycles, while after 100 cycles cluster formation is observed. Single dislocations within the clusters are clearly visible and the beginning of dislocation depletion in between the clusters is evident. The structures formed at strain amplitudes of 0.65% and 0.95% are characterized by a higher planar slip activity and higher dislocation density than at 0.35% strain amplitude. After 100 cycles with a strain amplitude of 0.65% pronounced veins which start to form networks are observed. The size of these veins is found to be 100–200 nm and their distances vary between 0.3 and 0.8 μm. The observed dislocation structures formed at a strain amplitude of 0.95% after 30 and 50 cycles are characterized by a transition from clusters to veins. The observed dislocation structures are



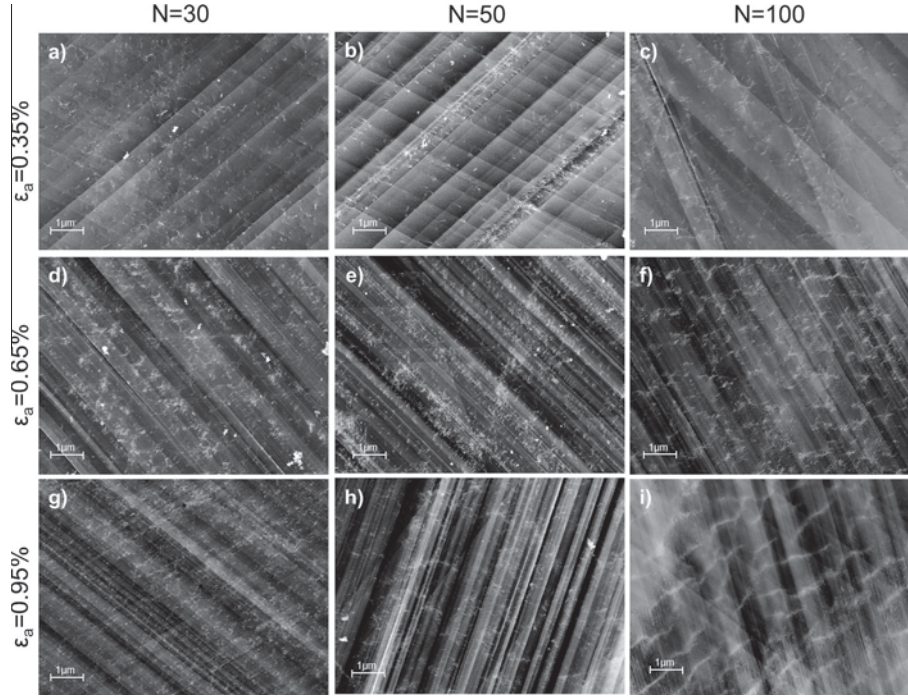


**Fig. 5.** Dislocation structures and slip traces observed in orientations close to  $\langle 112 \rangle // \text{LD}$ : (a)  $\varepsilon_a = 0.35\%$ ,  $N = 30$ ; (b)  $\varepsilon_a = 0.35\%$ ,  $N = 50$ ; (c)  $\varepsilon_a = 0.35\%$ ,  $N = 100$ ; (d)  $\varepsilon_a = 0.65\%$ ,  $N = 30$ ; (e)  $\varepsilon_a = 0.65\%$ ,  $N = 50$ ; (f)  $\varepsilon_a = 0.65\%$ ,  $N = 100$ ; (g)  $\varepsilon_a = 0.95\%$ ,  $N = 30$ ; (h)  $\varepsilon_a = 0.95\%$ ,  $N = 50$ ; (i)  $\varepsilon_a = 0.95\%$ ,  $N = 100$  (LD: loading direction).

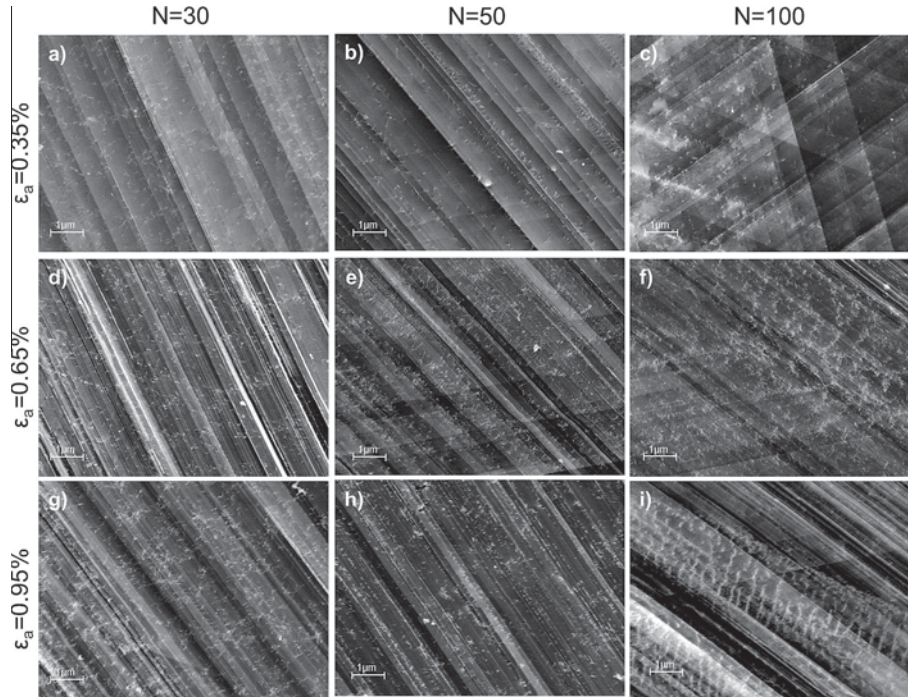


**Fig. 6.** Dislocation structures and slip traces observed in orientations close to  $\langle 122 \rangle // \text{LD}$ : (a)  $\varepsilon_a = 0.35\%$ ,  $N = 30$ ; (b)  $\varepsilon_a = 0.35\%$ ,  $N = 50$ ; (c)  $\varepsilon_a = 0.35\%$ ,  $N = 100$ ; (d)  $\varepsilon_a = 0.65\%$ ,  $N = 30$ ; (e)  $\varepsilon_a = 0.65\%$ ,  $N = 50$ ; (f)  $\varepsilon_a = 0.65\%$ ,  $N = 100$ ; (g)  $\varepsilon_a = 0.95\%$ ,  $N = 30$ ; (h)  $\varepsilon_a = 0.95\%$ ,  $N = 50$ ; (i)  $\varepsilon_a = 0.95\%$ ,  $N = 100$  (LD: loading direction).

heterogeneous: in some grains partially well-pronounced veins have formed, while in other regions individual dislocations and dislocation clusters are observed. The observed veins formed after 100 cycles at a strain amplitude of 0.65% (Fig. 8f) exhibit differently oriented segments. Orientations parallel to slip traces along  $(\bar{2}33)$  or  $(\bar{1}11)$  planes were

found as well as segments parallel to slip traces along  $(\bar{1}11)$  and  $(121)$  planes. Similar to the substructures observed at  $\varepsilon_a = 0.65\%$  and 100 cycles (Fig. 8f) veins with segments parallel to slip traces of  $(001)$ ,  $(03\bar{1})$ ,  $(11\bar{1})$  and  $(12\bar{1})$  or  $(\bar{1}\bar{1}3)$  planes are observed after 100 cycles at a strain amplitude of 0.95% (Fig. 8i).



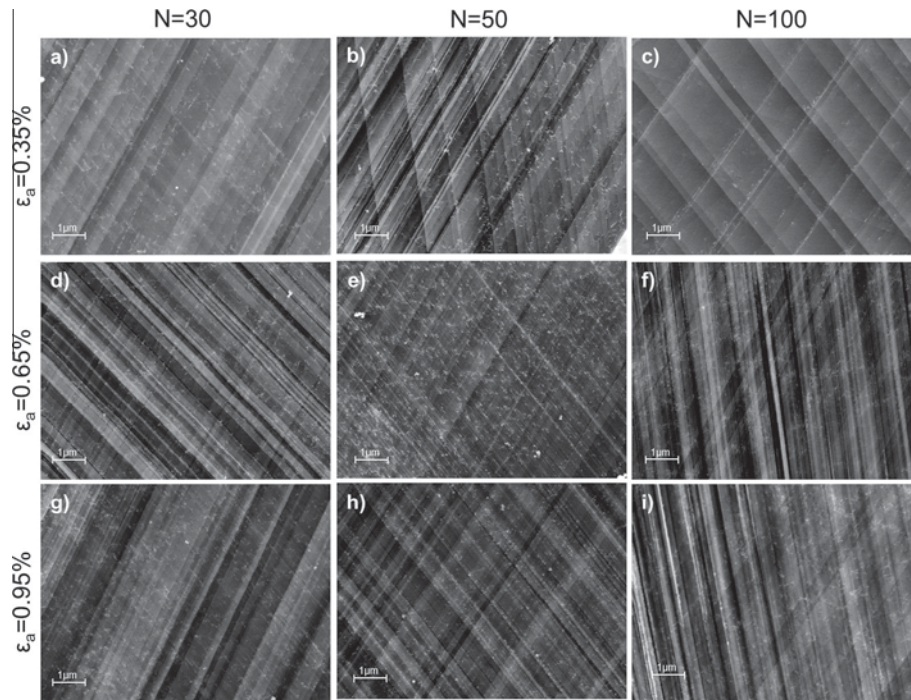


**Fig. 7.** Dislocation structures and slip traces observed in orientations close to  $\langle 012 \rangle // \text{LD}$ : (a)  $\varepsilon_a = 0.35\%$ ,  $N = 30$ ; (b)  $\varepsilon_a = 0.35\%$ ,  $N = 50$ ; (c)  $\varepsilon_a = 0.35\%$ ,  $N = 100$ ; (d)  $\varepsilon_a = 0.65\%$ ,  $N = 30$ ; (e)  $\varepsilon_a = 0.65\%$ ,  $N = 50$ ; (f)  $\varepsilon_a = 0.65\%$ ,  $N = 100$ ; (g)  $\varepsilon_a = 0.95\%$ ,  $N = 30$ ; (h)  $\varepsilon_a = 0.95\%$ ,  $N = 50$ ; (i)  $\varepsilon_a = 0.95\%$ ,  $N = 100$  (LD: loading direction).

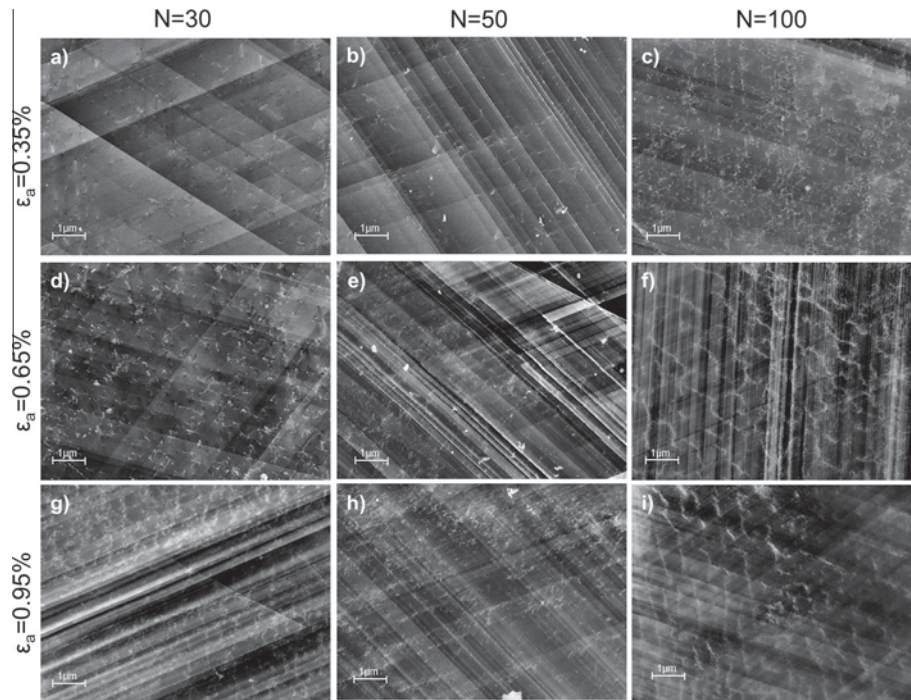


**Fig. 8.** Dislocation structures and slip traces observed in orientations close to  $\langle 111 \rangle // \text{LD}$ : (a)  $\varepsilon_a = 0.35\%$ ,  $N = 30$ ; (b)  $\varepsilon_a = 0.35\%$ ,  $N = 50$ ; (c)  $\varepsilon_a = 0.35\%$ ,  $N = 100$ ; (d)  $\varepsilon_a = 0.65\%$ ,  $N = 30$ ; (e)  $\varepsilon_a = 0.65\%$ ,  $N = 50$ ; (f)  $\varepsilon_a = 0.65\%$ ,  $N = 100$ ; (g)  $\varepsilon_a = 0.95\%$ ,  $N = 30$ ; (h)  $\varepsilon_a = 0.95\%$ ,  $N = 50$ ; (i)  $\varepsilon_a = 0.95\%$ ,  $N = 100$  (LD: loading direction).

### 3.3.5. $\langle 011 \rangle // \text{LD}$ multiple-slip orientation

The dislocation structures observed in grains with multiple-slip orientations close to  $\langle 011 \rangle // \text{LD}$  are presented in Fig. 9. No significant increase in planar dislocation activity was observed with increasing strain amplitude and cycle number as visible from the slip traces. A low density of indi-

vidual dislocations which are partially aligned with the traces of the active glide planes are found for the lowest strain amplitude of 0.35% for all cycle numbers. At strain amplitudes of 0.65% and 0.95% and up to 50 cycles the dislocations are mainly individually arranged and randomly distributed. After 50 cycles heterogeneous dislocation cluster

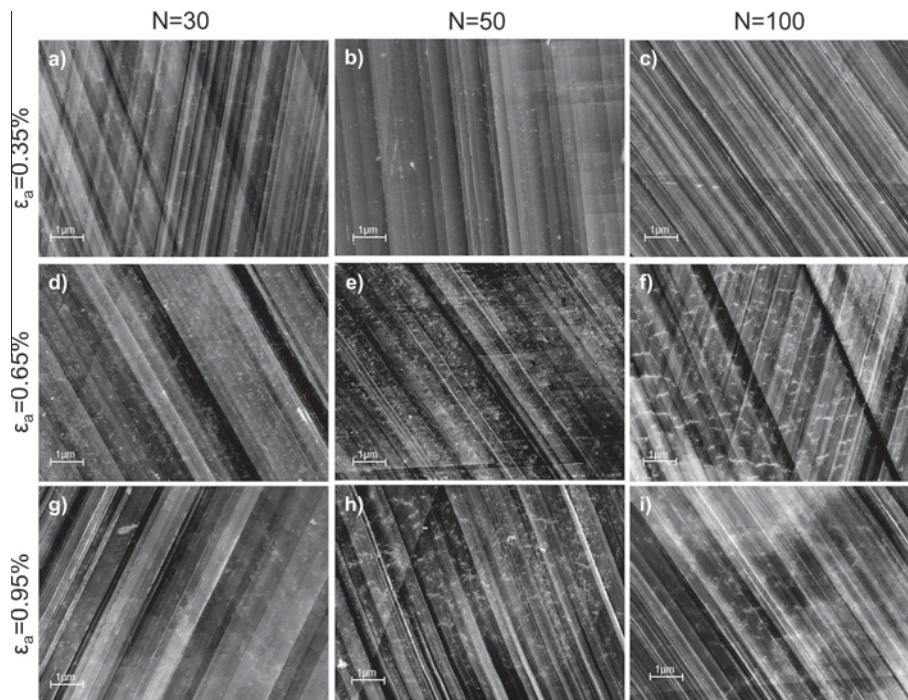


**Fig. 9.** Dislocation structures and slip traces observed in orientations close to  $\langle 011 \rangle // \text{LD}$ : (a)  $\varepsilon_a = 0.35\%$ ,  $N = 30$ ; (b)  $\varepsilon_a = 0.35\%$ ,  $N = 50$ ; (c)  $\varepsilon_a = 0.35\%$ ,  $N = 100$ ; (d)  $\varepsilon_a = 0.65\%$ ,  $N = 30$ ; (e)  $\varepsilon_a = 0.65\%$ ,  $N = 50$ ; (f)  $\varepsilon_a = 0.65\%$ ,  $N = 100$ ; (g)  $\varepsilon_a = 0.95\%$ ,  $N = 30$ ; (h)  $\varepsilon_a = 0.95\%$ ,  $N = 50$ ; (i)  $\varepsilon_a = 0.95\%$ ,  $N = 100$  (LD: loading direction).

formation is observed, accompanied by the onset of dislocation depletion between these clusters. The dislocation arrangements formed after 100 cycles mark the transition from dislocation clusters to veins. Due to their fragmented character, a detailed trace analysis of the vein orientation is not meaningful. No network formation is found. The observed veins have a size of 100–200 nm and a spacing of 400–800 nm. Compared to  $\langle 111 \rangle // \text{LD}$  multiple-slip orientation, the veins formed in  $\langle 011 \rangle // \text{LD}$  grains are less well pronounced.

### 3.3.6. $\langle 001 \rangle // \text{LD}$ multiple-slip orientation

Fig. 10 shows the dislocation arrangements formed in  $\langle 001 \rangle // \text{LD}$  multiple-slip orientations. For a strain amplitude of 0.35% individual dislocations which are mostly aligned with the slip traces are observed. With increasing cycle number, the dislocation density increases, but it is lower than in all other orientations studied. After 100 cycles at strain amplitudes of 0.35% and 0.65% singular and heterogeneously distributed dislocation clusters are observed (Fig. 10c and f). At a strain amplitude of 0.95% singular clusters with a size of 100–200 nm are formed after 30 cycles. With increasing cycle number the dislocation clusters become more pronounced and initial vein formation is observed at 0.95% strain amplitude. These veins (Fig. 10h) are parallel to  $(1\bar{1}1)$  and  $(\bar{1}10)$  plane traces and have a size of 100–200 nm and a spacing of 0.4–1.0  $\mu\text{m}$ .

## 4. Discussion

### 4.1. Validation of the experimental setup

To validate if the dislocation structures obtained with the ECCI technique are reliable and consistent with those

observed by other experimental means, the present ECCI results are compared with a recent transmission electron microscopy (TEM) study on dislocation structure formation during cyclic deformation in AISI316 stainless steel by Pham et al. [22]. Fig. 11 shows a comparison of the observed microstructures by TEM [22] and by ECCI (present study) at three different stages in the cyclic hardening curve.

This comparison clearly reveals the fidelity of the dislocation structures mapped by using the ECCI technique. By using ECCI the sample preparation can be performed prior to the actual deformation process, and hence slip traces are preserved. The ECCI method has several advantages in that context. First, it offers a very wide field of view. Second, no mechanical gradients and preparation artifacts from dimpling and TEM hole preparation occur. Third, the ECCI analysis – being a surface sensitive probing method – offers two types of complementary information sets, namely (i) the imaging of the deformation carriers (dislocations in the current case) together with the pattern substructures they form and (ii) the surface steps (slip traces) that they created at the sample surface (Fig. 4). Both aspects are essential for the interpretation of the observed structures, since they enable the simultaneous and correlative observation of the active slip planes, the resulting surface steps and the evolving dislocation substructures.

### 4.1.1. Role of inhomogeneous strain distribution

As visualized in Figs. 1c and 3, a significant difference between the global and the effective local strain amplitude was observed. As outlined in Section 3.2, it is assumed that these differences stem from locally heterogeneous micromechanical stress states in the polycrystalline samples. The average global strain amplitude was calculated to fall into the range between 0.55% and 0.65%, while the effective



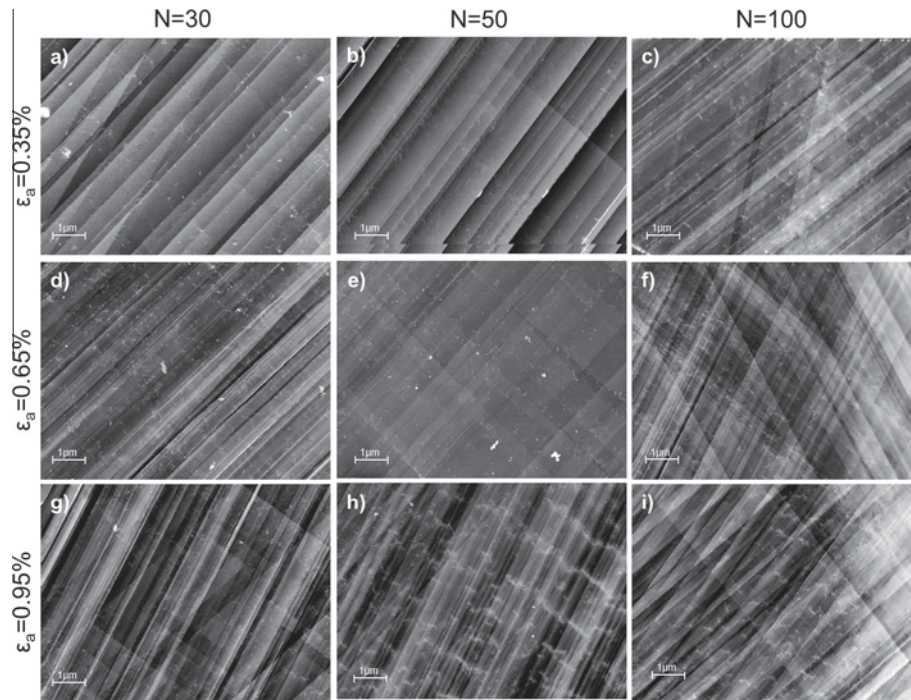


**Fig. 10.** Dislocation structures and slip traces observed in orientations close to  $\langle 001 \rangle // \text{LD}$ : (a)  $\varepsilon_a = 0.35\%$ ,  $N = 30$ ; (b)  $\varepsilon_a = 0.35\%$ ,  $N = 50$ ; (c)  $\varepsilon_a = 0.35\%$ ,  $N = 100$ ; (d)  $\varepsilon_a = 0.65\%$ ,  $N = 30$ ; (e)  $\varepsilon_a = 0.65\%$ ,  $N = 50$ ; (f)  $\varepsilon_a = 0.65\%$ ,  $N = 100$ ; (g)  $\varepsilon_a = 0.95\%$ ,  $N = 30$ ; (h)  $\varepsilon_a = 0.95\%$ ,  $N = 50$ ; (i)  $\varepsilon_a = 0.95\%$ ,  $N = 100$  (LD: loading direction).

	Hardening stage	Middle of softening stage	End of softening stage
a)			
b)			
Observed features	Mainly planar structures	Thick veins (premature walls) separated by long dislocation-free regions (channels)	Well-organized dislocation walls, thinner and denser compared to the middle

**Fig. 11.** Comparison of dislocation arrangements observed with ECCI and TEM [22] for different stages of cyclic hardening curves; the TEM data are taken from Ref. [22] (the TEM micrographs (b) are reprinted with permission from Elsevier).

local strain amplitude was in the range between 0.1% and 1.3%. This is a range of one order of magnitude. Taking into account that this difference is valid for each cycle, it is obvious that the difference in cumulated strain increases with each additional cycle. For example, Fig. 5 impressively visualizes the influence of the effective local strain amplitude. When considering that all micrographs shown in Fig. 5c, f and i originate from exactly the same specimen

which experienced cyclic deformation over 100 cycles and all micrographs show dislocation structures of the same orientation, the isolated influence of the effective local strain amplitude is evident. It should be considered that the average global strain was constant over all cycles, which is particularly the same as in strain controlled experiments. In these experiments only the average strain within the gauge length was measured. Without using an in situ DIC setup,

local deviations in the strain arising from buckling or misalignment of the specimen and from inhomogeneous material, texture and grain size effects remain undetected.

## 4.2. Microstructural evolution

### 4.2.1. Influence of strain amplitude and cycle number

The influence of the strain amplitude on the mechanical response and the dislocation arrangements in austenitic stainless steel (AISI 316) was investigated by several groups [2,4,14,21,22,24,42]. Generally, austenitic stainless steels subjected to cyclic straining show an initial hardening, followed by a softening and finally a subsequent stable response, termed saturation stage, before failure [2,4,14,21,22,24,42]. Increasing strain amplitude leads to an increase in the initial hardening rate and less pronounced softening. Our study focuses on low cycle fatigue in the softening regime ( $N = 30, 50$ ) and the beginning of the stable response regime ( $N = 100$ ), Fig. 2.

Gerland et al. [14] conducted a comprehensive investigation of the formation of dislocation structures as a function of the cyclic plastic strain amplitude after failure in 316L-type austenitic stainless steel. For very low strain amplitudes ( $6 \times 10^{-4}$ ) dislocation tangles were found to be the predominant structures. For intermediate strain amplitudes the fraction of tangles decreased continuously while the fraction of more complex structures, like walls, channels and cells, increased. For the highest investigated strain amplitude ( $1 \times 10^{-2}$ ) the planar structures disappeared and instead cell structures became the dominant feature. Dislocation labyrinth structures, persistent slip bands (PSBs) with ladders, microtwins and stacking faults were occasionally observed. The tendency that with higher strain amplitudes more complex dislocation structures formed was later confirmed also by several other authors [2,20,21,25].

Detailed studies of Pham et al. [22–24] and Mayama et al. [20,21] on the combined influence of cycle number and strain amplitude in low cycle fatigue on austenitic stainless steel show that increasing strain and/or cycle number increases the cumulative strain and accelerates the formation of more complex and dense substructures. They reported [22,23] that the microstructure during the hardening stage consisted mainly of planar structures in the form of stacking faults and dislocation tangles. The dislocation density increased at the end of the hardening stage and the tangles were more condensed. During the softening stage thick veins were observed, which developed into well-defined walls at the end of the softening stage. However, none of the above-mentioned studies considered crystallographic orientation effects on the formation of the dislocation substructures.

The same trends as outlined above [2,20–25] were also found in the present study: at low strain amplitudes (0.35%) individual dislocations and planar arrangements are predominantly observed, particularly in specimens loaded for 30 and 50 cycles. After 100 cycles dislocation clusters were observed in some orientations, indicating the analogous influence of strain amplitude and cycle number on the one hand and the influence of the orientation on the other hand. An intermediate strain amplitude of 0.65% is equivalent to a higher cumulative strain. Consequently, dislocation structures have to rearrange to comply with these strain boundary conditions. This process proceeds

by separation into dislocation-rich and dislocation-depleted regions [44]. When the cumulative strain increases by increasing the cycle number, the separation is more pronounced and the resulting vein structures become more condensed. For the highest local strain amplitude of 0.95% cluster formation occurs already after 30 cycles, corresponding to the global maximum of the cyclic hardening curve. At the beginning of the saturation stage after 100 cycles veins and channels were observed for most crystallographic orientations.

Besides strain amplitude, cycle number and orientation, the stacking fault energy (SFE) of the material effects the dislocation arrangements evolving during cyclic straining. Splitting of dislocations and the associated formation of planar dislocation structures are typical features for alloys with low stacking fault energy (e.g. Cu–16Al [45,46]). In contrast, the formation of dislocation bundles, veins, walls and cells are typically observed in materials with high stacking fault energy [2]. In addition, the occurrence of PSBs is also related to the stacking fault energy. Magnin et al. [19] reported a critical range for the SFE in fcc alloys between 20 and 30 mJ m<sup>-2</sup>, below which PSBs do not form. Austenitic stainless steel AISI 316L has a SFE of  $\sim 28$  mJ m<sup>-2</sup> [19] and is commonly observed to deform by planar slip [17,18].

### 4.2.2. Influence of crystallographic orientation

The influence of the orientation on dislocation structure formation during cyclic fatigue was studied mainly on Cu single crystals. Cu single crystals oriented for single slip form a “two-phase” substructure consisting of PSBs with a ladder structure embedded in a matrix consisting of loop patches or veins over a wide range of strain amplitudes [28,47,48]. In double slip oriented single crystals the formation of such two-phase structures ( $[\bar{1}12] // LD$ ), dislocation cells ( $[\bar{1}22] // LD$ ) and labyrinth structures ( $[012] // LD$ ) was observed [28,29].  $[\bar{1}11] // LD$  multiple-slip oriented Cu single crystals revealed dislocation arrangements consisting of matrix and PSB structures [47,49,50] where the matrix contained dislocation walls and channels and the PSBs were composed of dislocation cells and ladders [47,49]. For a low strain amplitude ( $8.8 \times 10^{-5}$ ) the dislocation structure after saturation consisted of labyrinth-like veins, while for a higher strain amplitude ( $4.0 \times 10^{-4}$ ) dislocation walls and misoriented cells were observed by Li et al. [50]. The formation of dislocation cells, dislocation ladders, veins and dislocation labyrinth structures in multiple-slip oriented  $[011] // LD$  Cu single crystals was observed after 16,000 cycles [51]. On the contrary, Li et al. [52] observed mainly PSB wall structures in  $[011] // LD$  oriented Cu single crystals at various strain amplitudes ( $1.1 \times 10^{-4}$ – $3.3 \times 10^{-3}$ ).  $[001] // LD$  multiple-slip oriented Cu single crystals form labyrinth structures when cyclically strained up to saturation at strain amplitudes between  $1.8 \times 10^{-3}$  and  $4 \times 10^{-3}$  [53,54].

In order to identify the activated slip systems, we performed a detailed analysis for each individual measurement using the OIM 6.2 software by TSL and TOCA [55]. Thus, the traces of the primary-, conjugate-, coplanar-, cross- and critical slip-system for each particular orientation were calculated [56]. However, quantitative correlation of the observed slip band density and the formed dislocation structures would require the quantification of the density of dislocations gliding on each individual slip band. Since



these data are not accessible with the current experimental methods, any conclusive correlations of slip band densities and formed dislocation structures would be speculative.

**4.2.2.1.  $\langle 112 \rangle // LD$  double-slip orientation.** Grains with an orientation close to  $\langle 112 \rangle // LD$  predominantly form complex structures such as veins in the low cycle regime. For this orientation cluster formation already starts after fewer cycles and at lower strain amplitudes compared to the other orientations considered. From previous studies conducted on Cu single crystals [29] of this orientation, it is known that the primary and conjugate slip systems strongly interact and form sessile Lomer–Cottrell locks (LCLs) [29].

All traces observed in grains with  $[\bar{1}12] // LD$  orientation (or crystallographic equivalent orientations) (Fig. 5) belong either to the primary  $(111)[\bar{1}01]$  or to the conjugate  $(\bar{1}\bar{1}1)[011]$  slip system (or crystallographic equivalent systems). No evidence for the activation of additional slip systems was found with one exception shown in Fig. 7e, where weak traces of the cross-slip system are observed. Consequently, the observed dislocation structures have formed by interactions between dislocations of the primary and the conjugate slip systems, which preferentially leads to the formation of sessile LCLs. Due to the sessile nature of these LCLs, a higher overall dislocation density is necessary to accommodate the applied strain. The formed LCLs act as obstacles against dislocation motion and thus promote the formation of dislocation networks. Consequently, the dislocation density increases rapidly and dislocation interactions and cluster formation start early and at low strain amplitudes. Accordingly, vein and channel formation in orientations close to  $\langle 112 \rangle // LD$  are much more pronounced when compared to the other double-slip orientations  $\langle 122 \rangle // LD$  and  $\langle 012 \rangle // LD$ .

**4.2.2.2.  $\langle 122 \rangle // LD$  double-slip orientation.** The highest stressed slip systems in  $[122] // LD$  orientations are the primary  $(111)[\bar{1}01]$  and the coplanar  $(111)[\bar{1}10]$  slip system. Thus, if only these slip systems were activated, only one trace should be observed. Our observations of the traces show only for low cycles ( $N \leq 30$ ) and a low strain amplitude (0.35%) one set of slip traces (Fig. 6). At higher cycle numbers ( $N = 50$ ,  $N = 100$ ) and higher strain amplitudes (0.65%, 0.95%) two to three sets of slip traces are present. It is observed that the slip traces of the primary and coplanar slip plane, respectively, are always most dominant, indicating that the additionally activated slip systems are activated at a later stage of loading. It is assumed that a critical cumulative strain is required before these additional slip systems become active. The product of the dislocation reactions of the primary and the coplanar slip system is glissile on the common primary slip plane; hence dislocation movement is not impeded. Furthermore, it is apparent that when more than one slip system is active, the observed dislocation interactions increase and more complex structures such as clusters and veins form.

**4.2.2.3.  $\langle 012 \rangle // LD$  double-slip orientation.** The dislocation structures observed in grains with  $\langle 012 \rangle // LD$  orientation exhibit less pronounced structures than in  $\langle 112 \rangle // LD$  and  $\langle 122 \rangle // LD$  orientations. All investigated grains show shear traces pertaining to the primary  $(111)[\bar{1}01]$  and the critical  $(\bar{1}\bar{1}1)[101]$  slip systems. Since the Burgers vectors of these two slip systems are perpendicular, not

much interaction other than the formation of jogs is expected. These jogs have practically no long-range elastic energy, and therefore the movement of subsequent dislocations is not much affected [57]. Consequently, no well-developed vein/channel-structures were observed, even for the highest combination of local strain amplitude and cycle number.

**4.2.2.4.  $\langle 111 \rangle // LD$  multiple-slip orientation.** Li et al. [32] attributed the formation of the observed cell structure in  $[\bar{1}11] // LD$  oriented fatigued Cu single crystals to the reaction of the primary and the coplanar secondary slip systems. Our results show traces of two or, in the case of Fig. 8e, three different slip planes, indicating the activity of more slip systems than the primary and coplanar slip systems. By calculating the six possible combinations of primary, conjugate, critical and cross-slip planes, it is found that in the case of two observed traces these traces belong to the primary and conjugate slip system, while in the case of three observed slip traces the third trace belongs to the cross-slip plane. Traces of the critical slip system were not observed. Assuming that the primary and the conjugate slip systems prevail during deformation, as observed in grains with  $\langle 112 \rangle // LD$  orientation, the formation of LCLs is favoured. A comparison of the structures formed in  $\langle 111 \rangle // LD$  orientations with those of the two other multiple-slip orientations  $\langle 011 \rangle // LD$  and  $\langle 001 \rangle // LD$ , respectively, supports this assumption, since the formation of more complex structures is advanced, in particular for low cycle numbers and strain amplitudes.

**4.2.2.5.  $\langle 011 \rangle // LD$  multiple-slip orientation.** The trace analysis for crystals with  $\langle 011 \rangle // LD$  orientations reveals a dominant dislocation activity on one slip plane. Only weak traces of a second (Fig. 9a, d, e, h and i) or third slip system (Fig. 9b, c and e) are found. These secondary traces were calculated in all cases to match the trace of the corresponding critical slip system. The formed veins in Fig. 9f are more pronounced than in Fig. 9i, although the cumulative strain is lower. This is probably due to the earlier activation of the critical slip system as visible from the more equally pronounced appearance of slip traces of those two systems. This aspect is further supported by the structures observed in Fig. 9h, where the cumulative strain is much lower than for the case shown in Fig. 9i. However, due to the higher activity of the critical slip system, indicated by the pronounced surface slip traces that it creates, dislocation interactions and networking are more advanced. Furthermore, it is assumed that the co-planar slip system must also be active, since the reaction of the primary and the critical slip system would have formed sessile jogs with no long range impact on the dislocation movement, as shown before for grains with  $\langle 012 \rangle // LD$  double slip orientation. However, due to the co-planar character, this system is not distinguishable from the primary slip system by mere trace observation. In  $\langle 011 \rangle // LD$  multiple-slip orientations the coplanar slip system is one of the possibly activated slip systems.

**4.2.2.6.  $\langle 001 \rangle // LD$  multiple-slip orientation.** For crystals with  $\langle 001 \rangle // LD$  multiple-slip orientation, eight slip systems on all four possible  $\{111\}$  slip planes are theoretical equally stressed [58]. Accordingly, a dominant primary slip system as observed for  $\langle 011 \rangle // LD$  orientations was

Cum. strain	0.42	0.70	0.78	1.14	1.30	1.40	1.90	2.60	3.80	
$N \times \epsilon_a$	30x 0.35%	50x 0.35%	30x 0.65%	30x 0.95%	50x 0.65%	100x 0.35%	50x 0.95%	100x 0.65%	100x 0.95%	
Orient.										
<112>	2	2	5	5-6	5	2	6	6	7-8	1 Only individual dislocations, low density
<122>	2	2	2-3	4	3	2	3	6	7	2 Only individual dislocations, medium density
<012>	2	2	2	3	3	1	3	6	6	3 Only individual dislocations, high density
<111>	1	1	2-3	6	4-5	3	4-5	7-8	7-8	4 (First) localized cluster
<011>	2	2	3	2	3-4	1	5	6-7	6-7	5 Medium pronounced cluster
<001>	1	1	2	4	2	2-3	6-7	5-6	6-7	6 Well pronounced cluster / pre-veins, still dislocations in between
										7 Well pronounced veins & dislocation free regions
										8 Pre-walls

Fig. 12. Classification of observed dislocation structures depending on orientation and cumulative strain.

not found. Instead, three or even four traces associated with different slip planes are almost equally activated. Consequently, the attribution of one individual trace to the primary slip system and the subsequent calculation of the traces pertaining to the critical, cross- and conjugate-slip systems, respectively, is not pertinent for this crystallographic orientation. Due to the high number of activated slip systems, dislocations are more equally distributed along the possible slip planes. This aspect decreases the possibility of dislocation reactions which impede the movement of dislocations; in particular, when cross-slip takes place. As a result, the formed dislocation arrangements are less dense than observed for  $\langle 111 \rangle // \text{LD}$  and  $\langle 011 \rangle // \text{LD}$  orientations, Fig. 10.

**4.2.2.7. Vein orientation.** The determination of the crystallographic directions of the observed veins was performed based on the double pseudo-polygonization (DPP) model proposed by Dickson et al. [59]. For AISI 316 stainless steel L'Espérance et al. [60] found wall orientations intermediate between  $\{100\}$  and  $\{210\}$  orientations. Furthermore, they identified  $\{111\}$  and  $\{211\}$  or  $\{311\}$  walls within a complex dipolar wall structure [60]. In addition, Kruml et al. [61] reported dislocation structures parallel to  $\{111\}$ .

In the current study, besides the reported  $\{100\}$  directions, veins parallel to various other traces were observed. It is therefore assumed, that during this early stage of fatigue, the veins elongate along various directions. It is further assumed that these veins transform into well pronounced walls after prolonged cycling. Dickson et al. [59] pointed out that some wall-orientations are theoretically possible, but mechanically unfavourable. Consequently, most vein segments observed in our study are assumed to merge into walls of one or two main orientations during prolonged cycling. This aspect is supported by the observation of wall segments oriented parallel to traces of  $\{111\}$  and  $\{211\}$  or  $\{311\}$  within a complex dipolar structure [60].

#### 4.2.3. Cumulative strain

The simultaneous investigation of three different influencing parameters as performed in this study reveals the complexity associated with the formation and evolution processes of dislocation structures during fatigue. In order to classify this complexity and to identify general trends and correlations, the structures are grouped into eight different classes where class 1 represents the lowest complexity and class 8 stands for well-developed complex substructure arrangements (Fig. 12). More specific, structures pertaining to classes 1 to 3 consist mainly of individual dislocations of

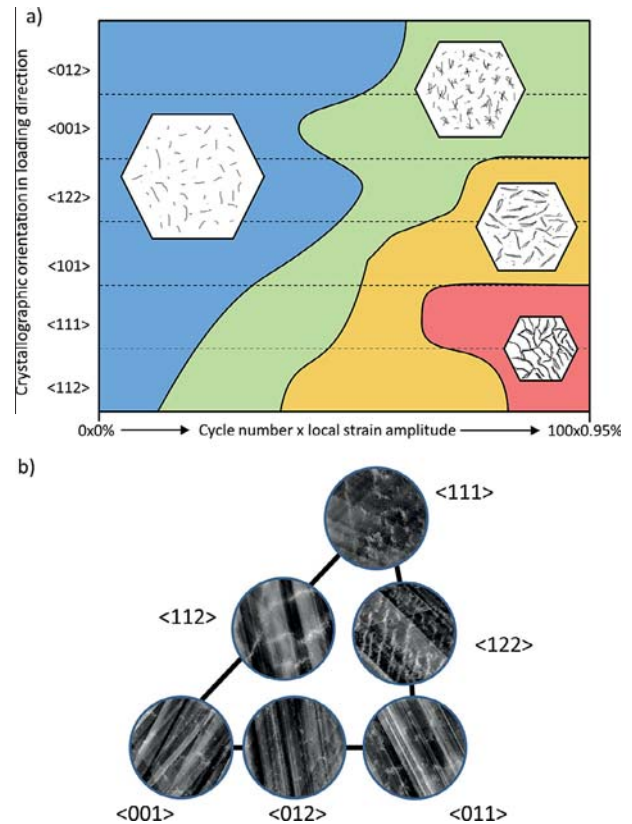


Fig. 13. (a) Dislocation structure formation map as a function of the combination of cycle number and strain amplitude and crystallographic orientation in loading direction; (b) final dislocation structures observed in different oriented grains for the highest investigated combination of strain amplitude and cycle number ( $N=100$ ,  $\epsilon_a=0.95\%$ ).

different density; classes 4 and 5 represent different stages of cluster formation; the transition from clusters to pre-veins is grouped into class 6; and well-pronounced veins and pre-mature walls are the main features in classes 7 and 8. For a better visualization of the different structure types, different colours are allocated to each class in Fig. 12. In addition, the combination of strain amplitude and cycle number is expressed by the cumulative strain  $\epsilon_{\text{cum}} = 4 \cdot \epsilon_a \cdot N$ , where  $\epsilon_a$  is the strain amplitude and  $N$  is the cycle number.

A general trend of increasing complexity of the formed dislocation structures with increasing cumulative strain is found, but with two exceptions. The structures observed



for a cumulative strain of 1.14 are much more complex than for the next higher cumulative strain of 1.30, whereas less complex arrangements are observed for a cumulative strain of 1.40, independent of the orientation. It is found that the cumulative strains of these two cases are formed by a combination of 30 cycles and a local strain amplitude of 0.95% (higher complexity) and 100 cycles and a local strain amplitude of 0.35% (lower complexity). Therefore, it is concluded that the formation of dislocation structures is more sensitive to the effective local strain amplitude than to the cycle number and the cumulative strain, respectively.

The evolution of dislocation patterns from individual dislocations, clustering and loose veins up to well-pronounced and condensed veins as a function of cumulative strain and orientation is summarized in Fig. 13a. The clear orientation dependence of dislocation structure formation is demonstrated in Fig. 13b, where the final structures for the highest investigated combination of strain amplitude and cycle number ( $N = 100$ ,  $\varepsilon_a = 0.95\%$ ) for each orientation are shown.

## 5. Conclusions

The method introduced here for the simultaneous investigation of the influence of crystallographic orientation, cycle number and strain amplitude on the dislocation structures in cyclically deformed AISI 316 polycrystalline stainless steel leads us to the following conclusions:

- (1) In situ strain observations by use of DIC reveal a heterogeneous distribution of the strain amplitude along the sample axis during cyclic deformation. We find that the local strain amplitude differs significantly from the average global strain amplitude and has a large influence on the formed dislocation structures.
- (2) Increasing strain amplitude and cycle number leads to an increased dislocation density and promotes the tendency to form complex structures such as veins.
- (3) A clear orientation dependence of the formed dislocation structures in polycrystalline stainless steel was found.
- (4) The effective local strain amplitude was found to have a higher influence on the formation of dislocation structures than the cumulative strain.

## Acknowledgements

The authors are grateful to the Deutsche Forschungsgemeinschaft (DFG) for funding the project SA 2251/2-1 “Constitutive modeling and microstructural validation for crystal plasticity finite element computation of cyclic plasticity in fatigue”.

## References

- [1] S.G. Hong, S.B. Lee, *Int. J. Fatigue* 899–910 (2004) 26.
- [2] K. Obrtlík, T. Kruml, J. Polák, *Mater. Sci. Eng., A* 1–9 (1994) 187.
- [3] G.P. Reddy, R. Sandhya, M. Valsan, K.B.S. Rao, *Int. J. Fatigue* 538–546 (2008) 30.
- [4] S.C. Roy, S. Goyal, R. Sandhya, S. Ray, *Nucl. Eng. Des.* 219–225 (2012) 253.
- [5] V. Srinivasan, M. Valsan, R. Sandhya, K.B.S. Rao, S. Mannan, D. Sastry, *Int. J. Fatigue* 11–21 (1999) 21.
- [6] H. Mughrabi, *Mater. Sci. Eng.* 207–223 (1978) 33.
- [7] H. Mughrabi, *Acta Metall.* 1367–1379 (1983) 31.
- [8] D. Kuhlmann-Wilsdorf, C. Laird, *Mater. Sci. Eng.* 137–156 (1977) 27.
- [9] D. Kuhlmann-Wilsdorf, C. Laird, *Mater. Sci. Eng.* 111–120 (1979) 37.
- [10] Z.S. Basinski, S.J. Basinski, *Prog. Mater. Sci.* 89–148 (1992) 36.
- [11] P. Li, S. Li, Z. Wang, Z. Zhang, *Prog. Mater. Sci.* 328–377 (2011) 6.
- [12] G. L'Espérance, J. Vogt, J. Dickson, *Mater. Sci. Eng.* 141–147 (1986) 79.
- [13] R. Alain, P. Violan, J. Mendez, *Mater. Sci. Eng., A* 87–94 (1997) 229.
- [14] M. Gerland, J. Mendez, P. Violan, B. Ait Saadi, *Mater. Sci. Eng., A* 83–95 (1989) 118.
- [15] M. Gerland, R. Alain, B. Ait Saadi, J. Mendez, *Mater. Sci. Eng. A* 68–86 (1997) 229.
- [16] M. Kamaya, *Int. J. Fatigue* 1081–1089 (2010) 32.
- [17] Y. Li, C. Laird, *Mater. Sci. Eng., A* 65–86 (1994) 186.
- [18] Y. Li, C. Laird, *Mater. Sci. Eng., A* 87–103 (1994) 186.
- [19] T. Magnin, C. Ramade, J. Lepinoux, L. Kubin, *Mater. Sci. Eng., A* 41–51 (1989) 118.
- [20] T. Mayama, K. Sasaki, Y. Narita, *Key Eng. Mater.* 49–52 (345–34) (2007) 6.
- [21] T. Mayama, K. Sasaki, M. Kuroda, *Acta Mater.* 2735–2743 (2008) 56.
- [22] M. Pham, C. Solenthaler, K. Janssens, S. Holdsworth, *Mater. Sci. Eng., A* 3261–3269 (2011) 528.
- [23] M. Pham, S. Holdsworth, *Procedia Eng.* 1069–1074 (2011) 10.
- [24] M. Pham, S. Holdsworth, K. Janssens, E. Mazza, *Int. J. Plast.* 143–164 (2013) 47.
- [25] N. Jin, C. Zhong, X. Chen, *Acta Metall. Mater.* 2141–2148 (1990) 38.
- [26] J. Vogt, J. Foct, C. Regnard, G. Robert, J. Dhers, *Metall. Trans. A* 2385–2392 (1991) 22.
- [27] J. Vogt, S. Degallaix, J. Foct, *Int. J. Fatigue* 211–215 (1984) 6.
- [28] N.Y. Jin, *Philos. Mag. A* 48 (1983) L33–L38.
- [29] N. Jin, A. Winter, *Acta Metall.* 989–995 (1984) 32.
- [30] X. Li, Z. Zhang, Z. Wang, S. Li, Y. Umakoshi, *Defect Diffus. Forum* 153–170 (188–19) (2001).
- [31] X. Li, Y. Umakoshi, B. Gong, S. Li, Z. Wang, *Mater. Sci. Eng., A* 51–59 (2002) 333.
- [32] P. Li, S. Li, Z. Wang, Z. Zhang, *Acta Mater.* 3281–3294 (2010) 58.
- [33] C. Buque, J. Bretschneider, A. Schwab, C. Holste, *Mater. Sci. Eng., A* 254–262 (2001) 300.
- [34] D. Raabe, M. Sachtleber, Z. Zhao, F. Roters, S. Zaefferer, *Acta Mater.* 3433–3441 (2001) 49.
- [35] D. Raabe, M. Sachtleber, H. Weiland, G. Scheele, Z. Zhao, *Acta Mater.* 1539–1560 (2003) 51.
- [36] A.J. Wilkinson, P.B. Hirsch, *Micron* 279–308 (1997) 28.
- [37] I. Gutierrez-Urrutia, D. Raabe, *Acta Mater.* 6449–6462 (2011) 59.
- [38] I. Gutierrez-Urrutia, D. Raabe, *Acta Mater.* 5791–5802 (2012) 60.
- [39] I. Gutierrez-Urrutia, S. Zaefferer, D. Raabe, *JOM* 1229–1236 (2013) 65.
- [40] I. Gutierrez-Urrutia, S. Zaefferer, D. Raabe, *Scripta Mater.* 737–740 (2009) 61.
- [41] S. Zaefferer, N.N. Elhami, *Acta Mater.* 20–50 (2014) 75.
- [42] A. Dutta, S. Dhar, S. Acharyya, *J. Mater. Sci.* 1782–1789 (2010) 45.
- [43] Y. Jiang, *Trans. ASME* 274–280 (2001) 123.
- [44] C. Laird, P. Charsley, H. Mughrabi, *Mater. Sci. Eng.* 433–450 (1986) 81.
- [45] C. Laird, S. Stanzl, R. de la Veaux, L. Buchinger, *Mater. Sci. Eng.* 143–154 (1986) 80.
- [46] H. Inui, S. Hong, C. Laird, *Acta Metall. Mater.* 2261–2274 (1990) 38.
- [47] T. Lepistö, V.-T. Kuokkala, P. Kettunen, *Mater. Sci. Eng.* 457–463 (1986) 81.

- [48] A.T. Winter, *Philos. Mag.* 719–738 (1974) 30.
- [49] T. Lepistö, V.-T. Kuokkala, P. Kettunen, *Scripta Metall.* 245–248 (1984) 18.
- [50] X.-W. Li, Y. Zhou, W.-W. Guo, G.-P. Zhang, *Cryst. Res. Technol.* 315–321 (2009) 44.
- [51] N.Y. Jin, *Philos. Mag. Lett.* 23–28 (1987) 56.
- [52] P. Li, Z. Zhang, S. Li, Z. Wang, *Mater. Sci. Eng., A* 2305–2312 (2010) 527.
- [53] N. Jin, A. Winter, *Acta Metall.* 1173–1176 (1984) 32.
- [54] Z. Wang, B. Gong, Z. Wang, *Acta Mater.* 1379–1391 (1997) 45.
- [55] S. Zaeferrer, *J. Appl. Crystallogr.* 10–25 (2000) 33.
- [56] R. Abbaschian, R.E. Reed-Hill, *Physical Metallurgy Principles*, fourth ed., Cengage Learning, 2009.
- [57] D. Hull, D. Bacon, *Introduction to Dislocations*, Butterworth–Heinemann, Oxford, 2011.
- [58] D. Raabe, Z. Zhao, F. Roters, *Scripta Mater.* 1085–1090 (2004) 50.
- [59] J. Dickson, J. Boutin, G. L’Espérance, *Acta Metall.* 1505–1514 (1986) 34.
- [60] G. L’Espérance, J. Vogt, J. Dickson, *ICSMA 7*, In: *Proceedings of the 7th International Conference on the Strength of Metals and Alloys*. Montreal, Canada: 1985. pp. 1423–1429.
- [61] T. Kruml, J. Polák, K. Obřtlík, S. Degallaix, *Acta Mater.* 5145–5151 (1997) 45.